Statistical properties of partially coherent polarization singular vector beams

Stuti Joshi,* Saba N. Khan,*,† P. Senthilkumaran, and Bhaskar Kanseri
Department of Physics, Indian Institute of Technology Delhi, Hauz Khas, New Delhi 110016, India

(Received 22 January 2021; accepted 14 April 2021; published 4 May 2021)

We investigate the statistical properties of partially coherent polarization singular beams embedded with a V-point polarization singularity. An analytical formula for the cross-spectral density matrix is derived for the family of partially coherent polarization singular vector beams (PSVBs) propagating through a paraxial ABCD optical system. It is observed that the far-field intensity profiles and the coherence-induced depolarization effect in partially coherent PSVBs depend on both the input spatial coherence length and the Poincaré-Hopf index (PHI) of the beam. Interestingly, it is found that in this process of coherence degradation, the polarization (Stokes, S_{12}) vortices are preserved. The depolarization is due to an enhanced unpolarized light field that in turn modulates the beam profile, the transverse distribution of the degree of polarization (DOP) and the degree of coherence (DOC). Furthermore, the Gaussian distribution of the DOC evolves into a non-Gaussian profile in the far-field with the number of ring dislocations equal to the magnitude of PHI of the beam. The degeneracy associated with the intensity profile, the Stokes intensity distribution, the DOP, and DOC profiles of these partially coherent PSVBs carrying opposite polarity of PHI are also discussed to complete this study. Subsequently, all of these findings are experimentally verified by generating a family of partially coherent PSVBs with controllable spatial coherence. The modulation of the spatial coherence length in the source plane leads to efficient control of its intensity, the DOC and DOP profiles on propagation, which are of importance in particle trapping, material thermal processing, free-space optical communications, and detection of a phase object.

DOI: 10.1103/PhysRevA.103.053502

I. INTRODUCTION

Polarization and coherence, the fundamental features of any light field, were considered to be independent until Wolf developed a unified theory of coherence and polarization [1,2]. This thought-provoking theory was then readily utilized to study the statistical properties—namely, the average intensity, degree of coherence (DOC), degree of polarization (DOP), and state of polarization (SOP)—of a partially coherent electromagnetic beam on propagation in free-space and atmospheric/oceanic turbulence [2–8]. Furthermore, it is claimed that partially coherent and partially polarized beams are more robust toward scintillation caused by atmospheric turbulence [9]. A partially coherent vortex beam has received a great deal of interest in recent years, thanks to the twofold benefits of partial coherence and vortex structure [10]. Partial coherence lowers the beam scintillation and beam wandering during propagation in random media, while the presence of a vortex phase enables beam-shaping from a doughnut to a Gaussian profile [11,12]. It is found that the statistical properties of the partially coherent vortex beam are influenced by both the spatial coherence and the topological charge of the beam [11–16].

Recently, more and more attention has been paid to polarization singular beams due to their potential applications in particle trapping [17–19], free-space optical communication [19–21], high-resolution microscopy [19,22], underwater communication [23], material processing [19,24], and photon entanglement [19,25,26]. Polarization singular beams endowed with V-point polarization singularity are generated by the superposition of two phase vortices possessing orthogonal polarization [27,28]. There are a number of different terms used in the literature for these V-point polarization singular beams, including vector vortex beams [29], cylindrical vector beams [30], Majorana-like vector beams [31], etc. The Poincaré-Hopf index (PHI: η) or the Stokes index (σ_{12}), where $\sigma_{12} = 2\eta$, is used to characterize these beams. Most of the research related to these beams is confined to fully coherent beams [27,32–34]. However, in recent reports it has been proposed that particles of different sizes and refractive indices can be trapped using a partially coherent radially polarized beam due to its unique state of polarization distribution and beam-shaping capability [35,36]. Furthermore, generic polarization singular vector beams (PSVBs) are found to be even more robust than scalar vortices for propagation in a turbulent medium [20,37]. For scalar vortices, the statistical properties are reported to be dependent on the topological charge of the beam. Thinking along these lines, it is anticipated that the PHI of the beam will govern the statistical properties of partially coherent PSVBs. There are few preliminary reports on the generation and characterization of generic partially coherent PSVBs (radially/azimuthally) [37–44]. However, the statistical characteristics of higher-index partially coherent PSVBs and their dependency on PHI are not yet explored. Therefore, a theoretical platform describing the complete statistical behavior of the family of isotropic partially coherent polarization

*These authors contributed equally to this work.
†sabaphotonics@gmail.com

 ©2021 American Physical Society

singular vector beams is developed as a part of this research. The partially coherent PSVBs exhibit coherence-induced depolarization effects [45] in contrast to the antidepolarization behavior demonstrated for partially coherent C-point polarization singular beams [46,47]. The statistical properties are also found to be dependent on both the input spatial coherence length and the PHI of the partially coherent PSVB.

The paper is organized as follows: In Sec. II, a generalized theoretical framework is developed to investigate the statistical properties of the whole family of partially coherent PSVBs. The theory predicts that the average intensity profile, the DOP and DOC distributions modulate over propagation. The far-field characteristics of these beams are fundamentally dependent on the PHI and the two-point correlation of the input beam. The experimental setup to synthesize and characterize these partially coherent PSVBs with different PHI indices is given in Sec. III. Section IV includes the experimental results, which are in good agreement with the theoretical predictions. The key findings of the study are concluded in Sec. V.

II. THEORETICAL DESCRIPTION: PARTIALLY COHERENT POLARIZATION SINGULAR VECTOR BEAM

In this article, the inhomogeneously polarized vector beams containing a V-point polarization singularity at the core of the beam are referred to as PSVBs. The beams carrying C-point polarization singularity are not considered here. The electric field of four major types [27,48] of PSVB (I/II/III/IV) can be written as a superposition of orthogonal orbital angular momentum (OAM) in orthogonal spin angular momentum (SAM) states as [27]

$$\begin{aligned}\mathbf{E}(\rho,\phi) &= \frac{\rho^{|m|}}{2}[e^{\pm im\phi}(\mathbf{x}-i\mathbf{y})\pm e^{\mp im\phi}(\mathbf{x}+i\mathbf{y})]|_{\mathrm{I/II}},\\ &= \frac{i\rho^{|m|}}{2}[\pm e^{\pm im\phi}(\mathbf{x}-i\mathbf{y})-e^{\mp im\phi}(\mathbf{x}+i\mathbf{y})]|_{\mathrm{III/IV}},\end{aligned} \tag{1}$$

where $\boldsymbol{\rho}=\rho_x\mathbf{x}+\rho_y\mathbf{y}$ with $\rho_x=\rho\cos\phi$, $\rho_y=\rho\sin\phi$, and $(\mathbf{x},\mathbf{y})$ are the unit vectors along the two orthogonal directions in the Cartesian coordinate system. m and ϕ are the topological charge and azimuthal angle, respectively. Here m determines the strength of the phase-gradient of the vortex beams, and it can take any integral value. The polarity $(+,-)$ of m depicts the handedness of the helical wavefront. By superposing two homogeneously polarized phase vortices having orthogonal polarizations, the information of the azimuthal phase-gradient can be encoded onto the cylindrically symmetric polarization distribution of the resulting beam. The in- or out-of phase superposition and the interchange of the orthogonal SAM (or OAM) state of two beams yield four distinct types of polarization distributions of a PSVB [27,48] corresponding to a fixed magnitude of topological charge ($|m|$). The endowed V-point polarization singularity exists at intensity null where the azimuth is indeterminate. These vector-field singularities are characterized by a Poincaré-Hopf index

$$\eta=\frac{1}{2\pi}\oint\nabla\gamma\cdot\mathbf{dl}, \tag{2}$$

where γ is the polarization azimuth of the linearly polarized states. η depicts the strength of the azimuth gradient, and it can take integral values. Corresponding to a particular η, there are two pairs of inhomogeneously polarized orthogonal basis states. For $\eta=+1$, orthogonal distributions are radial (type III) and azimuthal (type I), and likewise for $\eta=-1$, type II and type IV form the pair of orthogonal SOP distributions. Now, η can also have either $+ve$ (type I and type III) or $-ve$ (type II and type IV) polarity depending upon the counterclockwise (clockwise) sense of the azimuth gradient. This implies that for a V-point polarization singular beam having a particular $|\eta|$, there are four different types of polarization distributions considered here. One can refer to the figures presented in the later part of the article for the SOP distributions (types I–IV) corresponding to a fixed η.

Based on the unified theory [1], the coherence and polarization properties of a statistically stationary (in the wide sense), quasimonochromatic partially coherent PSVB beam can be determined from the 2×2 cross-spectral density (CSD) matrix as

$$\mathbf{W}(\boldsymbol{\rho}_1,\boldsymbol{\rho}_2,0)=\begin{pmatrix}\langle E_x^*(\boldsymbol{\rho}_1)E_x(\boldsymbol{\rho}_2)\rangle & \langle E_x^*(\boldsymbol{\rho}_1)E_y(\boldsymbol{\rho}_2)\rangle\\ \langle E_y^*(\boldsymbol{\rho}_1)E_x(\boldsymbol{\rho}_2)\rangle & \langle E_y^*(\boldsymbol{\rho}_1)E_y(\boldsymbol{\rho}_2)\rangle\end{pmatrix}, \tag{3}$$

where $\langle E_\alpha^*(\boldsymbol{\rho}_1)E_\beta(\boldsymbol{\rho}_2)\rangle$ $(\alpha=x,y;\ \beta=x,y)$ defines the field correlation between two transverse points $\boldsymbol{\rho}_1(\rho_1,\phi_1)$ and $\boldsymbol{\rho}_2(\rho_2,\phi_2)$. The angular brackets denote the ensemble average, and an asterisk denotes the complex conjugate. The partially coherent PSVBs are synthesized using a Gaussian Schell-model (GSM) type source [49] of beam waist σ and spatial coherence length $\delta_{\alpha\beta}$,

$$\langle E_\alpha^*(\boldsymbol{\rho}_1)E_\beta(\boldsymbol{\rho}_2)\rangle=\exp\left(-\frac{\boldsymbol{\rho}_1^2+\boldsymbol{\rho}_2^2}{4\sigma^2}\right)\exp\left(-\frac{(\boldsymbol{\rho}_2-\boldsymbol{\rho}_1)^2}{2{\delta_{\alpha\beta}}^2}\right). \tag{4}$$

In this study, the input GSM beam is considered to be isotropic, i.e., the spatial coherence length pertaining to different orthogonal electric field components is identical ($\delta_{xx}=\delta_{yy}=\delta_{xy}=\delta$). For a partially coherent PSVB of type I and type II, the elements of the CSD matrix, in the cylindrical coordinate system, at the source plane are expressed as

$$W_{0xx}^{\pm\eta}(\boldsymbol{\rho}_1,\boldsymbol{\rho}_2)|_{\mathrm{I/II}}=\cos(m\phi_1)\cos(m\phi_2)\xi(\boldsymbol{\rho}_1,\boldsymbol{\rho}_2), \tag{5a}$$

$$W_{0yy}^{\pm\eta}(\boldsymbol{\rho}_1,\boldsymbol{\rho}_2)|_{\mathrm{I/II}}=\sin(m\phi_1)\sin(m\phi_2)\xi(\boldsymbol{\rho}_1,\boldsymbol{\rho}_2), \tag{5b}$$

$$W_{0xy}^{\pm\eta}(\boldsymbol{\rho}_1,\boldsymbol{\rho}_2)|_{\mathrm{I/II}}=\pm\cos(m\phi_1)\sin(m\phi_2)\xi(\boldsymbol{\rho}_1,\boldsymbol{\rho}_2), \tag{5c}$$

$$W_{0yx}^{\pm\eta}(\boldsymbol{\rho}_1,\boldsymbol{\rho}_2)|_{\mathrm{I/II}}=\pm\sin(m\phi_1)\cos(m\phi_2)\xi(\boldsymbol{\rho}_1,\boldsymbol{\rho}_2), \tag{5d}$$

where $\xi(\boldsymbol{\rho}_1,\boldsymbol{\rho}_2)=\frac{(\rho_1\rho_2)^{|m|}}{(2\sigma)^{2|m|}}\exp\left(-\frac{\rho_1^2+\rho_2^2-2\rho_1\rho_2\cos(\phi_1-\phi_2)}{2\delta^2}\right)$ $\exp\left(-\frac{\rho_1^2+\rho_2^2}{4\sigma^2}\right)$. One can deduce the CSD matrix of the partially coherent PSVB of the other two types (III/IV) by inserting the appropriate field components in Eq. (3). The CSD matrix elements of these four types of partially coherent PSVBs are connected by the following relationship:

$$W_{0xx}^{\pm\eta}(\rho_1,\phi_1;\rho_2,\phi_2)|_{\mathrm{III/IV}}=W_{0yy}^{\pm\eta}(\rho_1,\phi_1;\rho_2,\phi_2)|_{\mathrm{I/II}}, \tag{6a}$$

$$W_{0yy}^{\pm\eta}(\rho_1,\phi_1;\rho_2,\phi_2)|_{\mathrm{III/IV}}=W_{0xx}^{\pm\eta}(\rho_1,\phi_1;\rho_2,\phi_2)|_{\mathrm{I/II}}, \tag{6b}$$

$$W_{0xy}^{\pm\eta}(\rho_1,\phi_1;\rho_2,\phi_2)|_{\mathrm{III/IV}}=-W_{0yx}^{\pm\eta}(\rho_1,\phi_1;\rho_2,\phi_2)|_{\mathrm{I/II}}, \tag{6c}$$

$$W_{0yx}^{\pm\eta}(\rho_1,\phi_1;\rho_2,\phi_2)|_{\mathrm{III/IV}}=-W_{0xy}^{\pm\eta}(\rho_1,\phi_1;\rho_2,\phi_2)|_{\mathrm{I/II}}. \tag{6d}$$

Within the paraxial approximation, the propagation properties of partially coherent PSVBs can be obtained by using the generalized Collins formula given by [50]

$$W_{\alpha\beta}(\mathbf{r}_1,\mathbf{r}_2,z)=\frac{1}{\lambda^2B^2}\int_0^{2\pi}\int_0^{2\pi}\int_0^{\infty}\int_0^{\infty}W_{0\alpha\beta}(\boldsymbol{\rho_1},\boldsymbol{\rho_2})\exp\left[\frac{ik}{B}[\rho_1r_1\cos(\theta_1-\phi_1)-\rho_2r_2\cos(\theta_2-\phi_2)]\right]$$
$$\times\exp\left[\frac{ikD}{2B}\left(r_2^2-r_1^2\right)-\frac{ikA}{2B}\left(\rho_1^2-\rho_2^2\right)\right]\rho_1\rho_2d\rho_1d\rho_2d\phi_1d\phi_2, \tag{7}$$

where $\alpha,\beta=x,y$; $k=2\pi/\lambda$, λ being the wavelength. $\mathbf{r}_1(r_1,\theta_1)$ and $\mathbf{r}_2(r_2,\theta_2)$ represent the coordinates of two transverse points of a partially coherent PSVB in the observation plane after propagating a distance z. A, B, C, and D are the transfer matrix elements of the optical system. Substituting Eq. (5) into Eq. (7), and after some tedious calculations, the elements of the CSD matrix of a partially coherent PSVB (type I/II) in the observation plane are obtained as

$$W_{xx}^{\pm\eta}(\mathbf{r}_1;\mathbf{r}_2;z)|_{\mathrm{I/II}}=-\Pi(r_1,r_2)\sum_{p=-\infty}^{\infty}\sum_{s=0}^{\infty}\exp[ip(\theta_1-\theta_2)]\left\{\frac{i^{2m}\exp(2im\theta_2)B_1(a_1,p)B_2(a_1,-2m+p)}{s!\Gamma(s+|-m+p|+1)(2\delta^2)^{2s+|-m+p|}}\right.$$
$$+\frac{B_1(a_2,p)B_2(a_2,p)}{s!\Gamma(s+|m+p|+1)(2\delta^2)^{2s+|m+p|}}+\frac{B_1(a_1,p)B_2(a_1,p)}{s!\Gamma(s+|-m+p|+1)(2\delta^2)^{2s+|-m+p|}}$$
$$\left.+\frac{i^{-2m}\exp(-2mi\theta_2)B_1(a_2,p)B_2(a_2,2m+p)}{s!\Gamma(s+|m+p|+1)(2\delta^2)^{2s+|m+p|}}\right\}, \tag{8a}$$

$$W_{yy}^{\pm\eta}(\mathbf{r}_1;\mathbf{r}_2;z)|_{\mathrm{I/II}}=\Pi(r_1,r_2)\sum_{p=-\infty}^{\infty}\sum_{s=0}^{\infty}\exp[ip(\theta_1-\theta_2)]\left\{\frac{i^{2m}\exp(2im\theta_2)B_1(a_1,p)B_2(a_1,-2m+p)}{s!\Gamma(s+|-m+p|+1)(2\delta^2)^{2s+|-m+p|}}\right.$$
$$-\frac{B_1(a_2,p)B_2(a_2,p)}{s!\Gamma(s+|m+p|+1)(2\delta^2)^{2s+|m+p|}}-\frac{B_1(a_1,p)B_2(a_1,p)}{s!\Gamma(s+|-m+p|+1)(2\delta^2)^{2s+|-m+p|}}$$
$$\left.+\frac{i^{-2m}\exp(-2mi\theta_2)B_1(a_2,p)B_2(a_2,2m+p)}{s!\Gamma(s+|m+p|+1)(2\delta^2)^{2s+|m+p|}}\right\}, \tag{8b}$$

$$W_{yx}^{\pm\eta}(\mathbf{r}_1;\mathbf{r}_2;z)|_{\mathrm{I/II}}=\pm i\Pi(r_1,r_2)\sum_{p=-\infty}^{\infty}\sum_{s=0}^{\infty}\exp[ip(\theta_1-\theta_2)]\left\{\frac{i^{2m}\exp(2im\theta_2)B_1(a_1,p)B_2(a_1,-2m+p)}{s!\Gamma(s+|-m+p|+1)(2\delta^2)^{2s+|-m+p|}}\right.$$
$$-\frac{B_1(a_2,p)B_2(a_2,p)}{s!\Gamma(s+|m+p|+1)(2\delta^2)^{2s+|m+p|}}+\frac{B_1(a_1,p)B_2(a_1,p)}{s!\Gamma(s+|-m+p|+1)(2\delta^2)^{2s+|-m+p|}}$$
$$\left.-\frac{i^{-2m}\exp(-2mi\theta_2)B_1(a_2,p)B_2(a_2,2m+p)}{s!\Gamma(s+|m+p|+1)(2\delta^2)^{2s+|m+p|}}\right\}, \tag{8c}$$

$$W_{xy}^{\pm\eta}(\mathbf{r}_1;\mathbf{r}_2;z)|_{\mathrm{I/II}}=W_{yx}^{*\pm\eta}(r_1,\theta_1;r_2,\theta_2)|_{\mathrm{I/II}}. \tag{8d}$$

In the above Eqs. (8a)– (8d), the descriptions of various functions are

$$\Pi(r_1,r_2)=\left(\frac{k^2}{4B^2(2\sigma)^{2|m|}}\right)\exp\left[\frac{ikD}{2B}\left(r_2^2-r_1^2\right)\right]\exp\left[-\frac{k^2r_1^2}{4M_1B^2}-\frac{k^2r_2^2}{4M_2B^2}\right], \tag{9}$$

$$B_1(a,b)=\frac{M_1^{-a/2}}{2\,b!}\Gamma\left(\frac{a+b}{2}\right)\left(\frac{k^2r_1^2}{4M_1B^2}\right)^{b/2}{}_1F_1\left[\frac{b-a}{2}+1;b+1;\frac{k^2r_1^2}{4M_1B^2}\right], \tag{10}$$

$$B_2(a,b)=\frac{M_2^{-a/2}}{2\,b!}\Gamma\left(\frac{a+b}{2}\right)\left(\frac{k^2r_2^2}{4M_2B^2}\right)^{b/2}{}_1F_1\left[\frac{b-a}{2}+1;b+1;\frac{k^2r_2^2}{4M_2B^2}\right], \tag{11}$$

$$M_{(1/2)}=\frac{1}{4\sigma^2}+\frac{1}{2\delta^2}\pm\frac{ikA}{2B}, \tag{12}$$

$$a_{(1/2)}=2s+m+2+|p\mp m|. \tag{13}$$

In this mathematical description, symbols $\Gamma(\cdot)$ and ${}_1F_1(\cdot;\cdot;)$ represent a Gamma and a Kummer functions, respectively. The subscripts (1/2) of Eqs. (12) and (13) are corresponding to the different sign (+/−) of the last term. In solving Eq. (7) for the CSD elements, we have used the following expansion and integral formulas [51,52]:

$$\exp\left[\frac{ik\rho_1\rho_2}{B}[\cos(\theta_1-\phi_1)]\right]=\sum_{l=-\infty}^{\infty}i^lJ_l\left(\frac{k\rho_1\rho_2}{B}\right)\exp\left[il(\theta_1-\phi_1)\right], \tag{14}$$

$$J_l(\chi) = \frac{(-i)^l}{2\pi}\int_0^{2\pi} \exp\left[il\theta_0 + i\chi\cos(\theta_0)\right], \tag{15}$$

$$\int_0^{2\pi} \exp\left[-in\phi_1 + N_1\rho_1\rho_2\cos(\phi_1-\phi_2)\right]d\phi_1 = 2\pi\exp(-in\phi_2)I_n(N_1\rho_1\rho_2), \tag{16}$$

$$I_n(N_1\rho_1\rho_2) = \sum_{s=0}^{\infty}\frac{1}{s!\Gamma(s+|n|+1)}\left(\frac{N_1\rho_1\rho_2}{2}\right)^{2s+|n|}, \tag{17}$$

$$\int_0^{\infty} x^q\exp(-\tau x^2)J_l(\nu x)dx = \frac{\nu^l\Gamma[(l+q+1)/2]}{2^{l+1}\tau^{(l+q+1)/2}\Gamma[l+1]}\,{}_1F_1\left(\frac{l+q+1}{2};l+1;-\frac{\nu^2}{4\tau}\right) \tag{18}$$

$${}_1F_1(a;b;c) = e^c\,{}_1F_1(b-a;b;-c). \tag{19}$$

Here $J_l(\cdot)$ and $I_n(\cdot)$ denote the lth- and nth-order regular and modified Bessel function of the first kind, respectively. Using Eq. (6), one can readily obtain the elements of the CSD matrix for the other two types of partially coherent PSVBs at the observation plane. The intensity at the observation plane z is expressed as

$$I(x,y,z) = \mathrm{Tr}\mathbf{W}^{\pm\eta}(\mathbf{r},\mathbf{r},z) = W_{xx}^{\pm\eta}(\mathbf{r},z) + W_{yy}^{\pm\eta}(\mathbf{r},z). \tag{20}$$

The CSD matrix of partially coherent PSVBs can be written as a sum of the CSD matrices of a polarized part ($\mathbf{W}_p^{\pm\eta}$) and an unpolarized part ($\mathbf{W}_u^{\pm\eta}$) as [2,3]

$$\mathbf{W}^{\pm\eta}(\mathbf{r},\mathbf{r},z) = \mathbf{W}_p^{\pm\eta}(\mathbf{r},\mathbf{r},z) + \mathbf{W}_u^{\pm\eta}(\mathbf{r},\mathbf{r},z), \tag{21}$$

where the matrices $\mathbf{W}_p^{\pm\eta}$ and $\mathbf{W}_u^{\pm\eta}$ are expressed as

$$\mathbf{W}_p^{\pm\eta}(\mathbf{r},\mathbf{r},z) = \begin{pmatrix} P(\mathbf{r},\mathbf{r},z) & R(\mathbf{r},\mathbf{r},z) \\ R^*(\mathbf{r},\mathbf{r},z) & Q(\mathbf{r},\mathbf{r},z)\end{pmatrix} \tag{22}$$

and

$$\mathbf{W}_u^{\pm\eta}(\mathbf{r},\mathbf{r},z) = \begin{pmatrix} U(\mathbf{r},\mathbf{r},z) & 0 \\ 0 & U(\mathbf{r},\mathbf{r},z)\end{pmatrix}. \tag{23}$$

The elements of CSD matrices of polarized and unpolarized parts are [3]

$$U(\mathbf{r},\mathbf{r},z) = \frac{1}{2}\left(W_{xx}^{\pm\eta}(\mathbf{r},\mathbf{r},z) + W_{yy}^{\pm\eta}(\mathbf{r},\mathbf{r},z) - \sqrt{\left(W_{xx}^{\pm\eta}(\mathbf{r},\mathbf{r},z) - W_{yy}^{\pm\eta}(\mathbf{r},\mathbf{r},z)\right)^2 + 4\left|W_{xy}^{\pm\eta}(\mathbf{r},\mathbf{r},z)\right|^2}\right), \tag{24}$$

$$P(\mathbf{r},\mathbf{r},z) = \frac{1}{2}\left(W_{xx}^{\pm\eta}(\mathbf{r},\mathbf{r},z) - W_{yy}^{\pm\eta}(\mathbf{r},\mathbf{r},z) + \sqrt{\left(W_{xx}^{\pm\eta}(\mathbf{r},\mathbf{r},z) - W_{yy}^{\pm\eta}(\mathbf{r},\mathbf{r},z)\right)^2 + 4\left|W_{xy}^{\pm\eta}(\mathbf{r},\mathbf{r},z)\right|^2}\right), \tag{25}$$

$$Q(\mathbf{r},\mathbf{r},z) = \frac{1}{2}\left(W_{yy}^{\pm\eta}(\mathbf{r},\mathbf{r},z) - W_{xx}^{\pm\eta}(\mathbf{r},\mathbf{r},z)\sqrt{\left(W_{xx}^{\pm\eta}(\mathbf{r},\mathbf{r},z) - W_{yy}^{\pm\eta}(\mathbf{r},\mathbf{r},z)\right)^2 + 4\left|W_{xy}^{\pm\eta}(\mathbf{r},\mathbf{r},z)\right|^2}\right), \tag{26}$$

$$R(\mathbf{r},\mathbf{r},z) = W_{xy}^{\pm\eta}(\mathbf{r},\mathbf{r},z). \tag{27}$$

The intensities of the corresponding polarized and unpolarized parts can be simply obtained as

$$I_j^{\pm\eta}(x,y) = \mathrm{Tr}\mathbf{W}_j^{\pm\eta}(\mathbf{r},\mathbf{r},z)\ \ (j=p,u). \tag{28}$$

To study the propagation properties of the partially coherent PSVBs, we assume that the beam generated at the source plane passes through a thin lens ($z=0$) of focal length f. The elements of the ABCD transfer matrix between source plane and observation plane are calculated as

$$\begin{pmatrix} A & B \\ C & D\end{pmatrix} = \begin{pmatrix} 1 & z \\ 0 & 1\end{pmatrix}\begin{pmatrix} 1 & 0 \\ -1/f & 1\end{pmatrix}\begin{pmatrix} 1 & f \\ 0 & 1\end{pmatrix} = \begin{pmatrix} 1-z/f & f \\ -1/f & 0\end{pmatrix}. \tag{29}$$

Equations (20) and (28) can then be used to study variation in the intensity distribution of the partially coherent PSVBs on propagation for distinct values of input spatial coherence length. In Fig. 1, the evolution of intensity distribution on propagation (polarized and unpolarized component's) of partially coherent PSVBs possessing $|\eta| = 1$, 2, and 3 for $\delta = 1.2$ mm is presented. As expected, it is observed that the dark hollow doughnut beam gradually transforms into a Gaussian beam profile on propagation. This transition from one profile-type to the other happens slowly in the case of higher-index partially coherent PSVBs carrying a bigger core-size. Moreover, the unpolarized intensity distribution of the generic partially coherent PSVB possesses a Gaussian profile even at the converging lens plane ($z=0$). On the contrary, the unpolarized intensity distributions of higher-index partially coherent PSVBs initially have a doughnut profile. The energy transfer from the high-intensity region into the dark core region on propagation results in the evolution of the

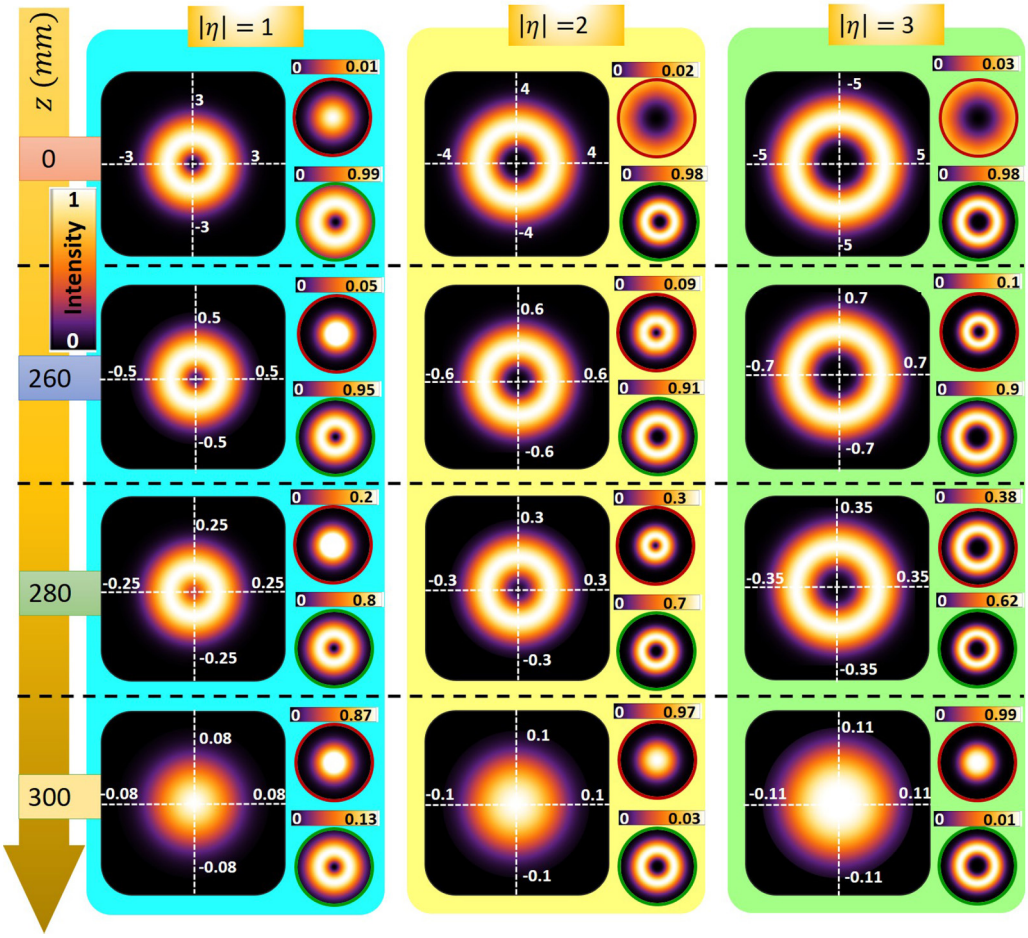

FIG. 1. Evolution of the intensity distribution of various index partially coherent PSVBs ($|\eta| = 1$, 2, and 3) on propagation. The far-field beam profiles are computed at propagation distances $z = 0$, 260, 280, and 300 mm for $\delta = 1.2$ mm. The intensity distribution of unpolarized (red-borderline) and polarized parts (green-borderline) are also shown with their respective color-maps.

Gaussian profile. Interestingly, the intensity distribution of the polarized part remains invariant for a particular η. Similar to the case of fully coherent completely polarized PSVBs, the core-size of the polarized intensity distribution of partially coherent PSVBs increases with increasing η (as can be seen from Fig. 1).

The total intensity and the DOP of the beam can also be interpreted in terms of power contained in the unpolarized and polarized parts of the beam. The normalized power of polarized and unpolarized components can be obtained from

$$\mathrm{P}_j^{\pm\eta}(z) = \frac{\iint I_j^{\pm\eta}\rho d\rho d\phi}{\iint I^{\pm\eta}\rho d\rho d\phi} \; (j = p, u), \tag{30}$$

where $\mathrm{P}_p^{\pm\eta}$ and $\mathrm{P}_u^{\pm\eta}$ represent the normalized powers of the polarized and unpolarized parts, respectively. Beam shaping of partially coherent PSVBs occurs on propagation and with changing input spatial coherence length. In Figs. 2(a) and 2(b), the variation in normalized power of unpolarized/polarized parts of focused partially coherent PSVBs has been plotted as a function of δ and z, respectively. The crossover point is marked with a filled-dot representing the semidepolarization point where the contribution from the polarized and unpolarized part is equal. For higher-index partially coherent PSVBs, this semidepolarization point shifts toward higher values of the spatial coherence length ($\delta|_{|\eta=1|} = 1.8$ mm $< \delta|_{|\eta=2|} = 3.1$ mm $< \delta|_{|\eta=1|} = 4$ mm). This indicates that the coherence-induced depolarization is more prominent in higher-index beams. Notably, only in the case of generic partially coherent PSVBs, the semidepolarization point corresponds to a flat-top profile [13]. This condition does not hold true for higher-index partially coherent PSVBs. A similar depolarization effect is observed in far-field propagation. It is found that the semidepolarization point occurs at a shorter propagation distance in higher-index partially coherent PSVBs ($z|_{|\eta=1|} = 292$ mm $> z|_{|\eta=2|} = 278$ mm $> z|_{|\eta=1|} = 264$ mm). For a fixed δ (or z), the polarized power content of a higher-index PSVB is always lesser, i.e., $\mathrm{P}_p|_{|\eta|=1} > \mathrm{P}_p|_{|\eta|=2} > \mathrm{P}_p|_{|\eta|=3}$.

The polarization properties of a partially coherent PSVB can be determined from Stokes parameters [S_j, ($j = 0, 1, 2, 3$)], which are related to CSD matrix elements as [2]

$$S_0(\mathbf{r}, z) = W_{xx}^{\pm\eta}(\mathbf{r}, \mathbf{r}, z) + W_{yy}^{\pm\eta}(\mathbf{r}, \mathbf{r}, z), \tag{31a}$$

$$S_1(\mathbf{r}, z) = W_{xx}^{\pm\eta}(\mathbf{r}, \mathbf{r}, z) - W_{yy}^{\pm\eta}(\mathbf{r}, \mathbf{r}, z), \tag{31b}$$

$$S_2(\boldsymbol{\rho}, z) = W_{xy}^{\pm\eta}(\mathbf{r}, \mathbf{r}, z) + W_{yx}^{\pm\eta}(\mathbf{r}, \mathbf{r}, z), \tag{31c}$$

$$S_3(\mathbf{r}, z) = i\big[W_{yx}^{\pm\eta}(\mathbf{r}, \mathbf{r}, z) - W_{xy}^{\pm\eta}(\mathbf{r}, \mathbf{r}, z)\big]. \tag{31d}$$

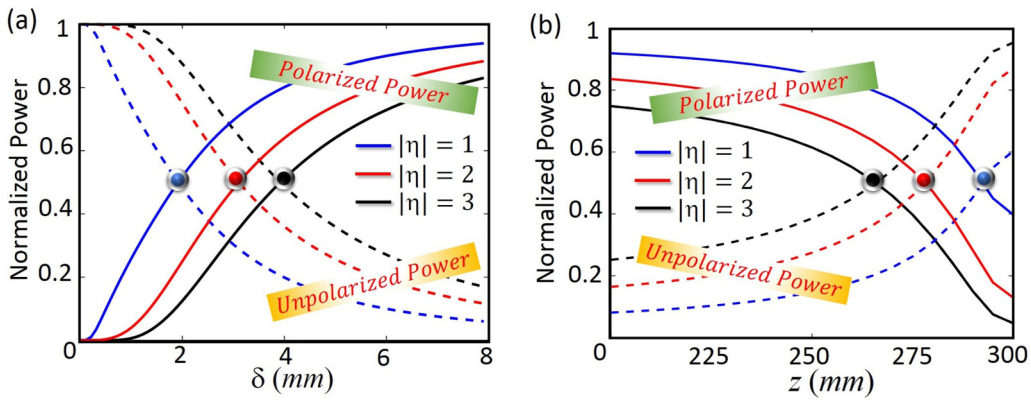

FIG. 2. Dependency of the polarized and unpolarized components' power of partially coherent PSVBs of $|\eta| = 1$ (blue curve), 2 (red curve), and 3 (black curve) on (a) spatial coherence length, δ and (b) propagation distance, z. The semidepolarization point is marked with a filled circle in each case.

For the analysis of V-point polarization singularities, one can construct a mathematical complex field distribution from Stokes parameter distribution as

$$S_{12}(\mathbf{r}, z) = S_1(\mathbf{r}, z) + iS_2(\mathbf{r}, z). \tag{32}$$

The Stokes phase corresponding to this constructed field represents the azimuth distribution

$$\phi_{12}(\mathbf{r}, z) = \tan^{-1}\left(\frac{S_2(\mathbf{r}, z)}{S_1(\mathbf{r}, z)}\right) = 2\gamma. \tag{33}$$

The phase vortices present in the Stokes field are identified as V-point polarization singularities with Stokes index $\sigma_{12} = 2\eta$. In such fields, $S_3 = 0$. The polarized component of the partially coherent PSVBs can have unique polarization distribution in the form of radial, azimuthal, flowerlike, spider-web, etc. [33,53], depending upon the OAM and SAM states of the superposing beams. The Stokes intensity corresponding to the polarized field possesses a doughnut intensity profile and can be mathematically described as

$$|S_{12}(\mathbf{r}, z)|^2 = |S_1(\mathbf{r}, z)|^2 + |S_2(\mathbf{r}, z)|^2. \tag{34}$$

The degree of polarization can be defined as [2]

$$\mathcal{P}^{\pm\eta}(\mathbf{r}, z) = \frac{I_p(r, z)}{I(r, z)} = \frac{\sqrt{S_1^2(\mathbf{r}, z) + S_2^2(\mathbf{r}, z) + S_3^2(\mathbf{r}, z)}}{S_0(\mathbf{r}, z)}. \tag{35}$$

Intensity results indicate that self-shaping of the beam is attributed to the change in the unpolarized intensity distribution and its strength in the transverse plane. Subsequently, the DOP, which is a measure of the polarized contribution of the total intensity, is investigated. In Fig. 3, the variation of transverse DOP profiles corresponding to $\delta = 2.5$ and 1.5 mm at different propagation distances is shown. The DOP distribution possesses a doughnut profile whose line-scan depicts that the on-axis point always has a zero-DOP due to the absence of a polarized field. The DOP increases gradually in the radial direction and falls off toward the edge of the beam. The maximum value of DOP depends upon the strength of the correlation between orthogonal electric field components at a single point. The single point correlation is not disturbed much for short propagation distances, and therefore coherence-induced depolarization is found to be prominent only in the far-field propagation. It is interesting to note that as the two-point correlation (coherence length) at the source plane decreases, the maximum extent of single-point correlation also reduces in the observation plane. Such a DOP-modulation is expected for inhomogeneously polarized vector beams because the correlation between two transverse points in the source plane depends on the state of polarization at these points as well [54,55]. In the case of higher-index partially coherent PSVBs, the DOP deteriorates $[\mathcal{P}_{\max}^{|\eta|=1}(\delta, z) > \mathcal{P}_{\max}^{|\eta|=2}(\delta, z) > \mathcal{P}_{\max}^{|\eta|=3}(\delta, z)]$ more quickly. This is due to the fact that the higher-index partially coherent PSVBs are highly unstable and even a slight perturbation dissociates these beams into unit-index generic PSVBs [56,57], which are spatially uncorrelated. Therefore, higher-index partially coherent PSVBs are more robust toward atmospheric turbulent scintillation leading to better information preservation in free-space optical communication [9]. Additionally, the DOP-dip becomes wider in a higher-index partially coherent PSVB due to the bigger dark-core region. The width of the dip also increases on decreasing spatial coherence length, which can be readily observed in the far-field plane. The DOP profile of a partially coherent PSVB is much different from a phase-vortex beam or a vortex-induced radially polarized beam. Scalar phase vortices have a nonvarying transverse distribution of the DOP due to the homogeneous SOP distribution [58]. However, the vortex-induced radially polarized beam possesses a transverse DOP-distribution in which the on-axis DOP is nonzero and its strength is governed by the topological charge of the added vortex [46,47,58]. So, here rather than coherence-induced depolarization, an opposite antidepolarization effect was observed.

Now, we theoretically investigate the coherence properties of the partially coherent PSVBs on propagation. The degree of coherence of a beam at two transverse points $\mathbf{r}_1\,(x_1, y_1)$ and $\mathbf{r}_2\,(x_2, y_2)$ is mathematically expressed as [2]

$$|\mu(\mathbf{r}_1, \mathbf{r}_2, z)| = \frac{\mathrm{Tr}[\mathbf{W}^{\pm\eta}(\mathbf{r}_1, \mathbf{r}_2, z)]}{\sqrt{\mathrm{Tr}[\mathbf{W}^{\pm\eta}(\mathbf{r}_1, \mathbf{r}_1, z)]}\sqrt{\mathrm{Tr}[\mathbf{W}^{\pm\eta}(\mathbf{r}_2, \mathbf{r}_2, z)]}}. \tag{36}$$

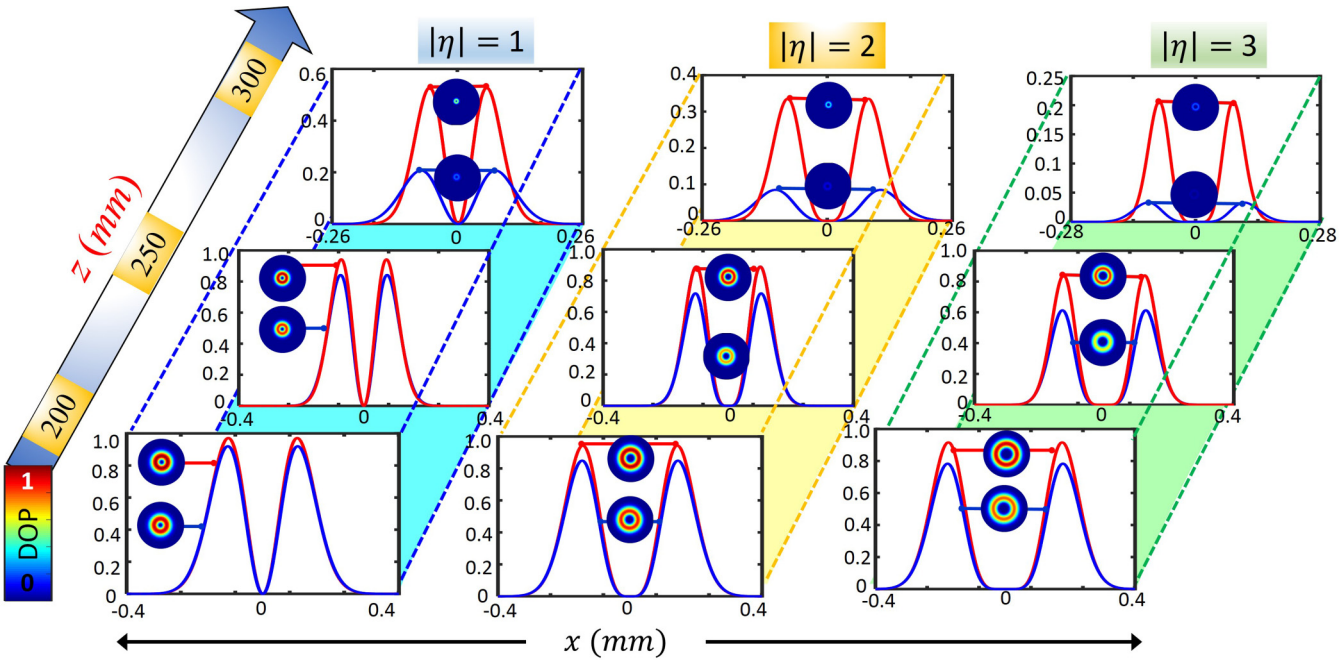

FIG. 3. Dependency of the DOP profile of various index partially coherent PSVBs ($|\eta| = 1$, 2, and 3) on propagation distance. The evolution of the DOP is investigated considering two δ values 2.5 mm (red curve) and 1.5 mm (blue curve) at $z = 200$, 250, and 300 mm. The DOP-distribution is shown as an inset in respective line-scans. It can be readily observed that the coherence-induced DOP degradation is more prominent in a higher-index partially coherent PSVBs.

Equation (36) together with Eqs. (8a) and (8d) can be used to determine the modulus of DOC at distance z. In Fig. 4, the variation of modulus of DOC at several propagation distances corresponding to spatial coherence length $\delta = 1.2$ and 2.3 mm is plotted for partially coherent PSVBs having $|\eta| = 1$, 2, and 3, respectively. At the source plane, all the partially coherent PSVBs ($|\eta| = 1, 2, 3$) possess a Gaussian distribution of DOC. The spread of the distribution is governed by the spatial coherence length of the input beam. Interestingly, it is observed that the DOC-profile changes from a Gaussian to a non-Gaussian profile over propagation. The multi-ring structure formed at the far-field also contains the information of the PHI ($|\eta|$) of the beam. The number of dark-rings (ring-dislocations) is as many as $|\eta|$ of the partially coherent PSVB. These ring-dislocations appear gradually over propagation. The dislocations where the DOC is zero depict no correlation between two transverse points. At these positions, the phase of DOC becomes undetermined. This transformation suggests the conversion of phase singularity of PSVBs into correlation singularities. It is found that the visibility of the interference pattern, which is a measure of the modulus of DOC, depends on both the polarization and coherence properties at the source-plane [55]. The significance of the outermost bright ring (the strength of the extreme end of the side-lobes) increases in a more correlated field having a larger δ value. In addition, the spread of DOC-distribution is more for a higher-index partially coherent PSVB due to their inherent diffraction properties. The elements of the matrix $\mathbf{W}_p(\mathbf{r}, \mathbf{r}, z)$ [Eqs. (25)–(27)] define the polarization state at the respective spatial point in the beam cross-section, i.e., the size, shape, and the orientation of the polarization ellipses. Considering the equivalence of polarized matrix ($\mathbf{W}_p^{\pm\eta}$) elements with the spatially varying polarized field at the observation plane to be composed of $E_x^{\text{obs}}(\mathbf{r}, z)$ and $E_y^{\text{obs}}(\mathbf{r}, z)$ components, one can obtain the master equation governing the SOP distribution of polarization ellipses in the beam cross-section as

$$Q(\mathbf{r}, z)\big(E_x^{\text{obs}}(\mathbf{r}, z)\big)^2 - 2\,\text{Re}[R(\mathbf{r}, z)]E_x^{\text{obs}}(\mathbf{r}, z)E_y^{\text{obs}}(\mathbf{r}, z) + P(\mathbf{r}, z)\big(E_y^{\text{obs}}(\mathbf{r}, z)\big)^2 = \{\text{Im}[R(\mathbf{r}, z)]\}^2. \tag{37}$$

It is noteworthy that here $E_x^{\text{obs}}(\mathbf{r}, z)$ and $E_y^{\text{obs}}(\mathbf{r}, z)$ are time-independent parts of the complex monochromatic component at each of the spatial points. $P(\mathbf{r}, z)$, $Q(\mathbf{r}, z)$, and $R(\mathbf{r}, z)$ are defined by Eqs. (25)–(27). The phase difference at the respective positions is given by $\Delta\phi = \arg[R(\mathbf{r}, z)]$. Now to obtain the azimuth (γ) and the magnitude of major (A_+) and minor (A_-) axes for each of the polarization ellipses in the distribution, we will eliminate the second term by arbitrary rotation of the coordinate system (with respect to each transverse position).

After some simplification, one can get the parameters characterizing the inhomogeneous polarization ellipse distribution as

$$\gamma(\mathbf{r}, z) = \frac{1}{2}\tan^{-1}\left(\frac{2\,\text{Re}\big[W_{xy}^{\pm\eta}\big]}{W_{xx}^{\pm\eta} - W_{yy}^{\pm\eta}}\right) = \frac{1}{2}\tan^{-1}\left(\frac{S_2}{S_1}\right), \tag{38}$$

$$A_{\pm}^2(\mathbf{r}, z) = \frac{\sqrt{\big(W_{xx}^{\pm\eta} - W_{yy}^{\pm\eta}\big)^2 + 4\big|W_{xy}^{\pm\eta}\big|^2}}{2} \pm \frac{\sqrt{\big(W_{xx}^{\pm\eta} - W_{yy}^{\pm\eta}\big)^2 + 4\,\text{Re}\big[W_{xy}^{\pm\eta}\big]^2}}{2}. \tag{39}$$

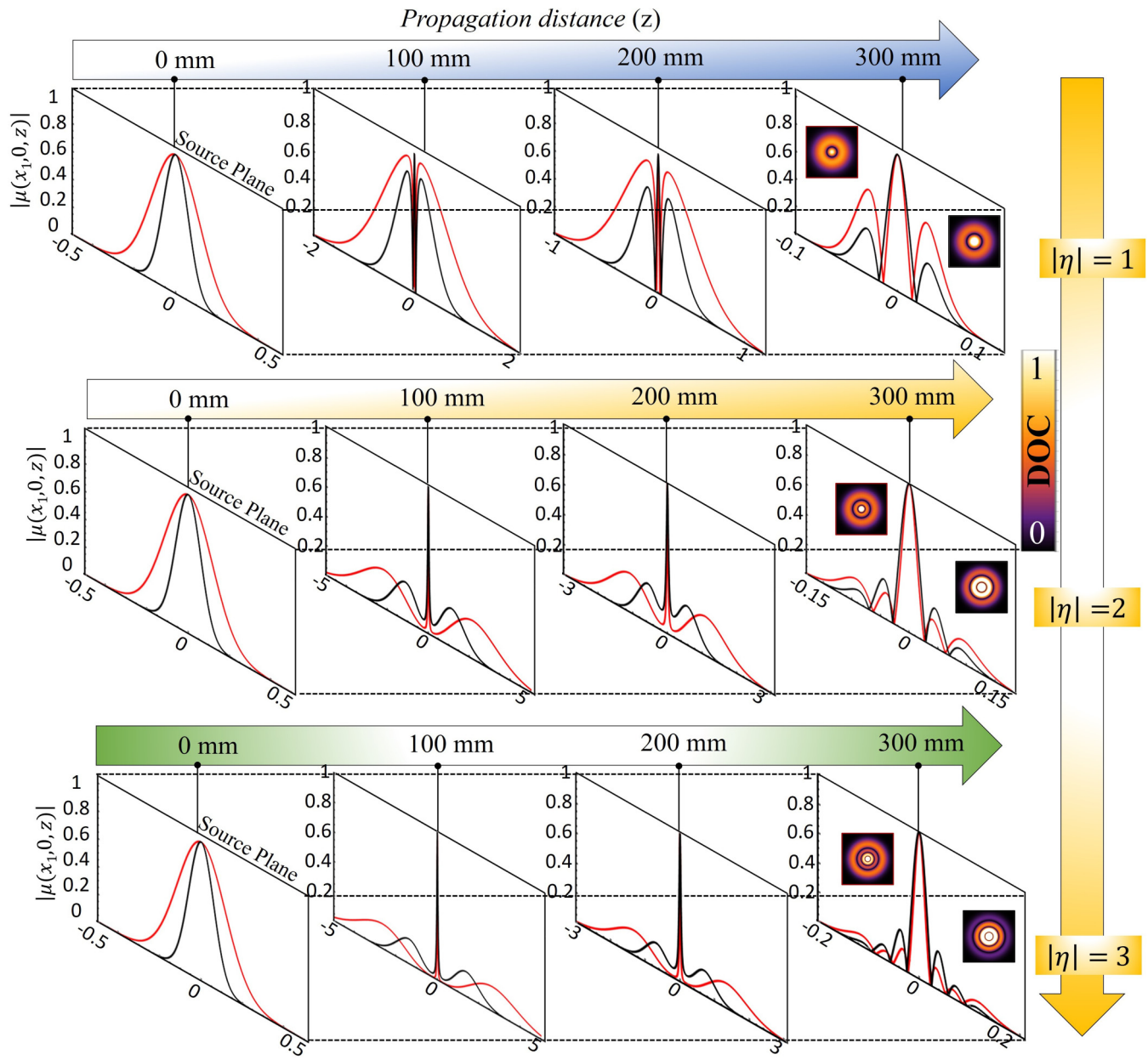

FIG. 4. Far-field DOC characteristics of partially coherent PSVBs having $|\eta| = 1$, 2, and 3 respectively. The evolution of the DOC on propagation is shown as the line-scan at $z = 0$, 100, 200, and 300 mm. The input spatial coherence length is considered to be $\delta = 2.3$ mm (red curve) and $\delta = 1.2$ mm (black curve). The focused DOC contains ring-dislocations ($= |\eta|$), which are shown as insets.

Here, the arguments $(\mathbf{r}, z)$ of $W_{\alpha\beta}$ are omitted due to space constraints. It is seen that the azimuth in the observation plane is half of the Stokes phase, and the magnitude of the respective minor axis is zero over the entire beam cross-section. This implies that the polarization distribution is invariant on changing the input spatial correlation of an isotropic source ($\delta_{xx} = \delta_{yy} = \delta_{xy} = \delta$). In Fig. 5, the polarization distributions and degeneracies present in the PSVBs are shown for a fixed $\delta = 1.2$ mm. For all four types of partially coherent PSVBs of a fixed η, the focused intensity profile, Stokes intensity profile, DOP distribution, and DOC distribution are degenerate. Actually, these distributions are dependent upon the OAM states of the superposing beams [see Eq. (1)]. The invariant profile of the Stokes intensity distribution (although the magnitude deteriorates uniformly) indicates that the polarization vortices are preserved in the polarized part of the intensity in this process of coherence-induced degradation. The charge (σ_{12}) of the Stokes phase vortex depicts the magnitude and polarity of the partially coherent PSVB. For a higher-index partially coherent PSVB, the SOP distribution is flower (spider-web) patterned for positive (negative) polarity of η, and the number of petals (sector-of-web) is $2[\eta - 1]$ ($2[\eta + 1]$). The invariance of SOP distribution suggests that one can control the longitudinal and transverse trapping ranges of the particles

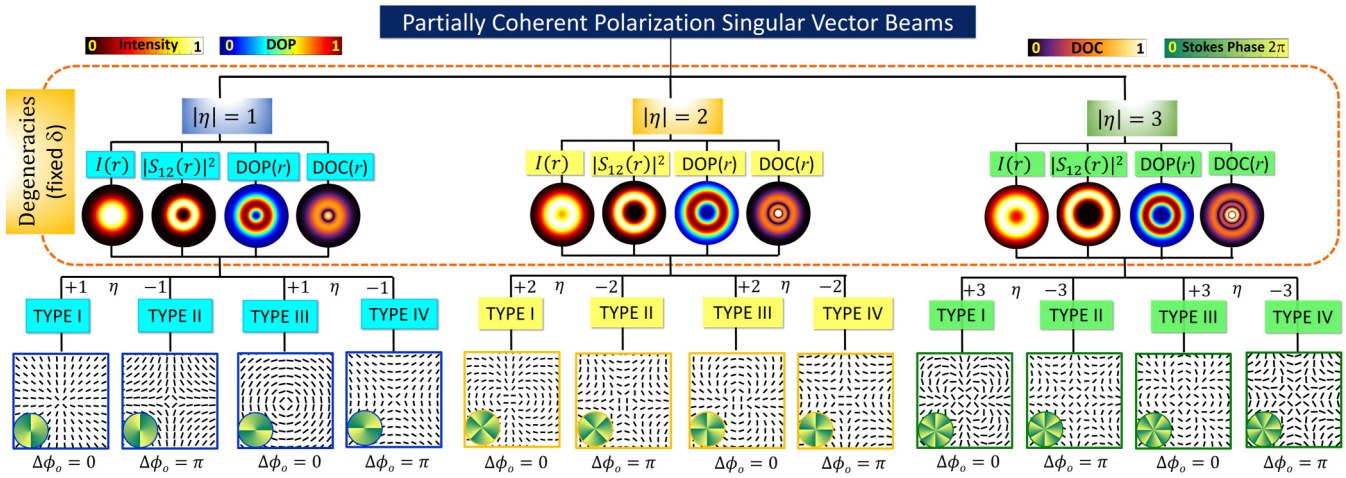

FIG. 5. Schematic describing the inherent degeneracies present in the partially coherent PSVBs. Beams with $|\eta| = 1$, 2, and 3 are considered to carry out this study. The SOP distributions and the Stokes phases of the polarized component of partially coherent PSVBs for all four types of V-point polarization singularities are shown. The SOP distribution is preserved in the polarized part of the beam even on reducing the spatial coherence length ($\delta = 1.2$ mm) of the beam.

through the input spatial coherence length, appropriate beam index (η), and type (SOP distribution) [36].

III. SYNTHESIS OF PARTIALLY COHERENT PSVBs

The schematic of our experimental setup used to generate and investigate the statistical properties of partially coherent PSVBs is shown in Fig. 6. A linearly polarized light-beam of a He-Ne laser ($\lambda = 632.8$ nm) is collimated with a combination of MO-PH and lens L_1. The collimated beam is then directed by lens L_2 toward a rotating ground glass diffuser (RGGD) to obtain a spatially incoherent light source. The RGGD and spatially varying wave-plate (SWP) are placed at the front and back focal plane of lens L_3, respectively, such that a partially spatially coherent beam falls at the SWP [59]. The SWP embeds the requisite polarization distribution on the incoming beam while maintaining unit-DOP across the beam profile. The spatial coherence length at SWP can be calculated from $\delta = \frac{3.832\lambda f_3}{2\pi d}$ [59], where λ is the wavelength of light, f_3 is the focal length of lens L_3, and d is the beam-size at the diffuser plane. Partially coherent light with different spatial coherence length is obtained by varying the beam-size (d) at the diffuser plane by translating lens L_2. The generated beam is then focused by a lens L_4 of focal length $f_4 = 300$ mm to study its far-field propagation properties. The input polarizer is rotated by $\frac{\pi}{2}$ in order to obtain the counterpart of the or-

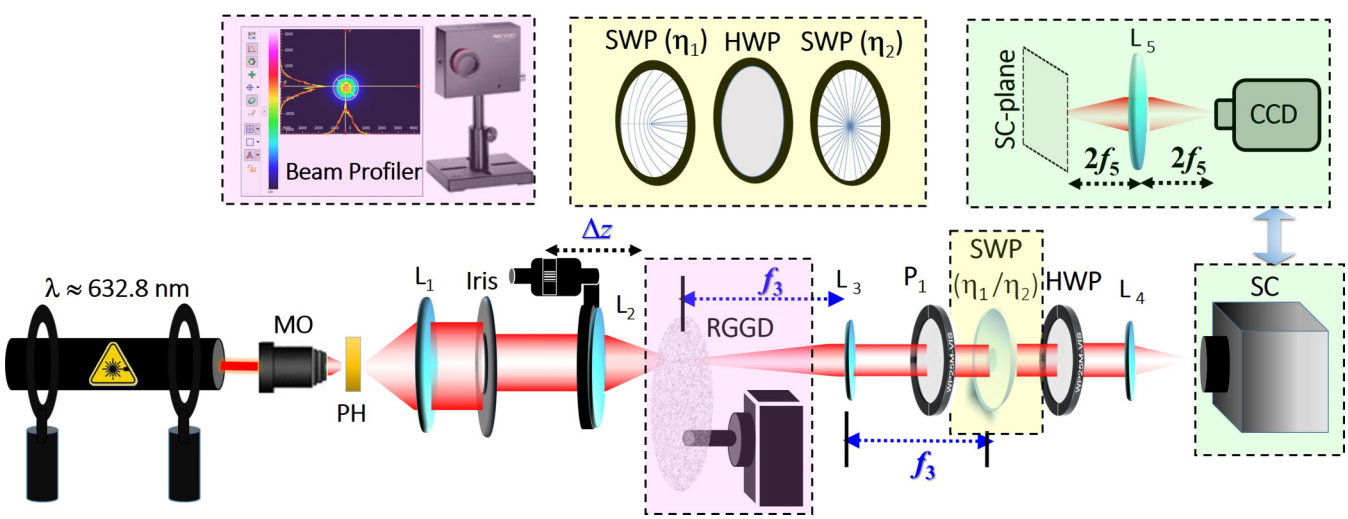

FIG. 6. Schematic of the experimental setup used to synthesize and investigate the far-field propagation characteristics of partially coherent PSVBs. Abbreviations are as follows: L_1, L_2, L_3, L_4, L_5: lens; MO: microscope objective; PH: pinhole; P: polarizer; SWP: spatially varying wave plate; HWP: half-wave plate; RGGD: rotating ground glass diffuser; CCD: charged coupled device; and SC: Stokes camera. Translating lens L_2 provides the control over the spatial coherence length of the generated partially coherent PSVBs. The SOP distribution of the output beam is governed by the orientation of the polarizer and the HWP. The PSVB of $|\eta| = 3$ is generated using two SWPs of $|\eta| = 1$ and 2 in concatenation with a HWP as shown in the inset (yellow background). The SC plane is imaged onto the CCD camera using the configuration shown in the green-background inset. RGGD is replaced with a beam profiler to measure the focal spot size (pink background inset).

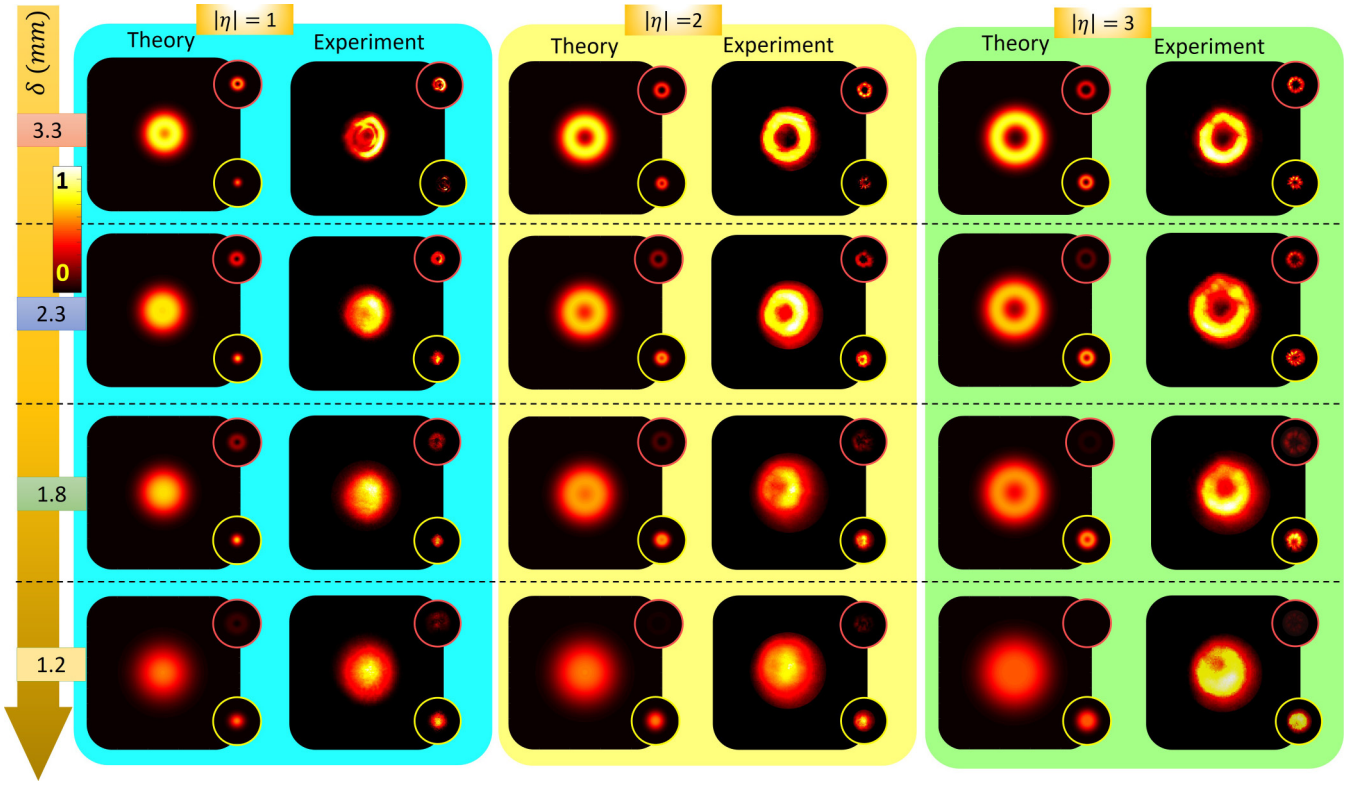

FIG. 7. Experimental plots of focused intensity of partially coherent PSVBs of PHI $|\eta| = 1$ (cyan background), $|\eta| = 2$ (yellow background), and $|\eta| = 1$ (green background) for different values of δ. The insets encircled with red and yellow are the polarized and unpolarized parts of the total intensity. The beam-shaping aspect with reducing δ can be readily observed. The transformation from a doughnut to a Gaussian beam profile occurs slowly for higher η partially coherent PSVBs.

thogonal pair (type I $\leftrightarrow$ type III) of the respective PSVBs. An additional half-wave plate (HWP) is used to generate negative polarity counterparts (type II and type IV) of the PSVBs [60]. In this way, all four types of partially coherent PSVBs of a particular $|\eta|$ are obtained. The Stokes parameters (S_j; $j = 0$ to 3) of the partially coherent PSVBs are recorded by Stokes camera (SALSA, Bossa Nova Technologies, USA) having a resolution of 1040×1040 pixels. PSVBs of $|\eta| = 1$ and 2 are generated by directly illuminating SWP of order 1 and 2, respectively (SWP, Model: WPV10L-633, Thorlabs), while a PSVB of $|\eta| = 3$ is generated using SWPs of $\eta = 1$ and 2 in concatenation with HWP (see the inset of Fig. 6). The fast axis angle distributions of SWP having $\eta = 1$ and 2 are shown in the inset of Fig. 6.

IV. EXPERIMENTAL: PROPAGATION CHARACTERISTICS OF PARTIALLY COHERENT PSVBs

In this section, we present our experimental results pertaining to the statistical properties (intensity distribution, DOP profile, DOC profile, and SOP distributions) of the partially coherent PSVBs and we justify/verify the claims made on the basis of theoretical formulation detailed in Sec. II. The experimentally obtained focused intensity profiles of partially coherent PSVBs having $|\eta| = 1$, 2, and 3 with input spatial coherence length as a variable parameter are shown in Fig. 7. The intensity profiles of the corresponding polarized (red borderline) and unpolarized (yellow borderline) parts are also plotted. With the decrease in spatial coherence length, the intensity profile changes from doughnut to flat-top and finally evolves to Gaussian distribution. Different beam profiles of PSVBs are useful for different applications; for example, flat-top PSVBs show their usefulness in high-resolution confocal microscopy [61], and doughnut beam profiles are effective in particle trapping. For all $|\eta|$'s, the intensity profile of the polarized part remains a doughnut. On the other hand, the unpolarized part has a Gaussian distribution for $|\eta| = 1$ irrespective of the value of input spatial coherence length. But, for $|\eta| = 2$ and 3, the unpolarized part has a dark-core at the center that keeps on shrinking with the decreasing input spatial coherence length and finally acquires a Gaussian distribution. A similar effect has been observed with varying z as depicted in Fig. 8 and theoretically claimed in Fig. 1. A detailed explanation of observed intensity profile variation is given in Sec. II. The experimentally obtained transverse DOP profiles for $|\eta| = 1$, 2, and 3 with propagation distances are shown in Fig. 9. It can be observed that the DOP-variation is insignificant for short distances. But near to the focus ($\geqslant$270 mm), the maximum DOP value is governed by the input spatial coherence length [45]. For the presented result in Fig. 9 with $\delta = 1.8$ mm, the maximum values of DOP are obtained as 0.35, 0.18, and 0.08 for $|\eta| = 1$, 2, and 3, respectively. As predicted from the theory, the width of the DOP-dip increases with the increasing PHI of the partially coherent PSVB.

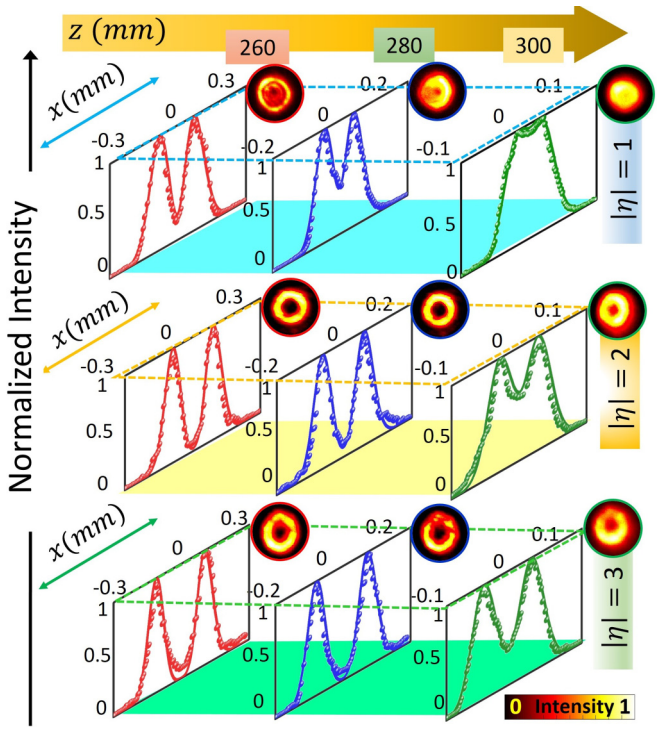

FIG. 8. Changes observed in the intensity profile in far-field propagation of partially coherent PSVBs ($|\eta| = 1$, 2, and 3) are presented as the line-scan of intensity distribution for $z = 260$, 280, and 300 mm. The input spatial coherence length was fixed at $\delta = 2.3$ mm. Here the solid line is the predicted theoretical profile, and the filled spheres are the experimentally obtained data points. The profile transition rate from a doughnut to a Gaussian is slower for a higher-index partially coherent PSVB.

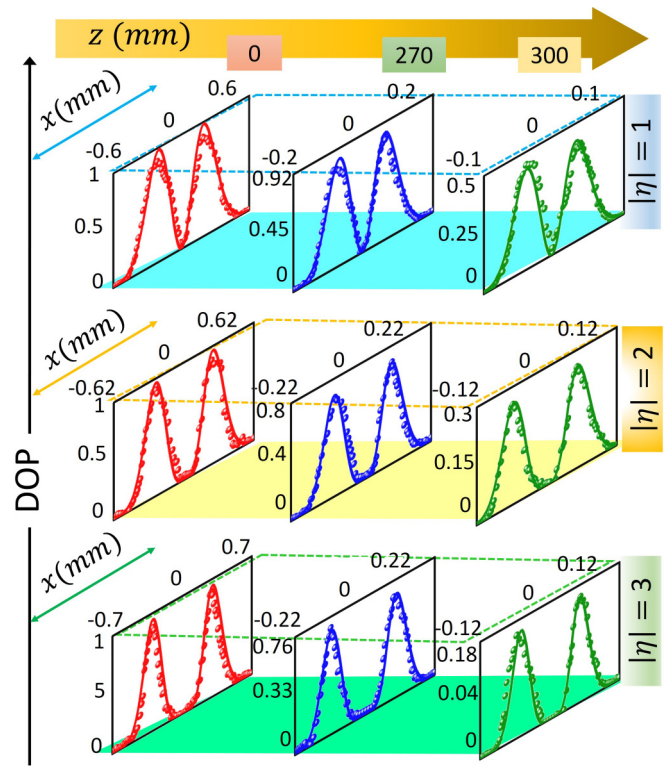

FIG. 9. Changes observed in the DOP in far-field propagation of partially coherent PSVBs ($|\eta| = 1$, 2, and 3) are presented as the line profile of a DOP for $z = 0$, 270, and 300 mm. These DOP profiles are extracted for the input $\delta = 2.3$ mm. Here the solid line is the predicted theoretical profile, and filled spheres are the experimentally obtained data points. It can be observed that the depolarization of higher-index partially coherent PSVBs is more rapid with a wider zero-dip profile.

The dotted inset (green background in Fig. 6) of the experimental setup is used to measure the degree of coherence of the focused partially coherent PSVB. The focused beam is passed through a lens L_5 and the instantaneous intensity is recorded using a charge-coupled device (CCD). The distance from Stokes camera (SC) plane to lens (L_5) and from lens to CCD is kept at $2f_5$ to image the SC plane onto the CCD camera. In this imaging process, the degree of coherence at the CCD plane is the same as that of the SC plane. In our experiment, we have recorded 2000 instantaneous and continuous images for a particular value of input coherence length $\delta = 2.3$ mm. The recorded images are then processed in MATLAB to determine the square of the DOC. The square of the DOC is obtained using the formula [43]

$$|\mu(\mathbf{r}_1, \mathbf{r}_2, f_5)|^2 = \frac{\frac{1}{N}\sum_{u=1}^{N} I^{(u)}(x_1, y_1) I^{(u)}(0,0)}{I^{(v)}_{\text{avg}}(x_1, y_1) I^{(v)}_{\text{avg}}(0,0)} - 1, \quad (40)$$

where $I^{(u)}_{\text{avg}}(x_1, y_1) = \frac{1}{N}\sum_{u=1}^{N} I^{(u)}(x_1, y_1)$ and $I^{(u)}_{\text{avg}}(0,0) = \frac{1}{N}\sum_{u=1}^{N} I^{(u)}(0,0)$. The modulus of DOC of the focused partially coherent PSVBs with $|\eta| = 1$, 2 and 3 is plotted in Fig. 10. As detailed in Sec. II, DOC distribution shows ring dislocations that are equivalent to $|\eta|$ of the beam. Next, in Fig. 11, the experimentally obtained SOP distributions and Stokes phases of all four types of partially coherent PSVB of $\eta = 1$, 2, and 3 are shown for two different δ values (3.8 and 2.3 mm). Notably, all four types of partially coherent PSVBs of a particular $|\eta|$ corresponding to a fixed δ have a degenerate intensity and Stokes-intensity distributions. It can be readily observed that the SOP distribution remains invariant upon changing the input spatial coherence length. This suggests that the phase and polarization vortices are preserved in the polarized part of the intensity. In addition, it is anticipated that the invariant polarization distribution with a tunable transverse-DOP can provide an additional degree of freedom in applications projected for such PSVBs in a classical [27,36,62] and a quantum domain [63].

V. CONCLUSION

In this article, we have investigated the statistical properties of partially coherent polarization singular vector beams of various indices $|\eta| = 1$, 2, and 3. The well-known four types of V-point polarization singular beam are considered corresponding to a particular $|\eta|$ to carry out this study. A generalized analytical theoretical framework for the cross-spectral density matrix is developed to investigate the various statistical properties, namely intensity, total power, degree of polarization, degree of coherence, and state of polarization distributions for the whole family of partially coherent PSVBs propagating through a paraxial ABCD optical system. The

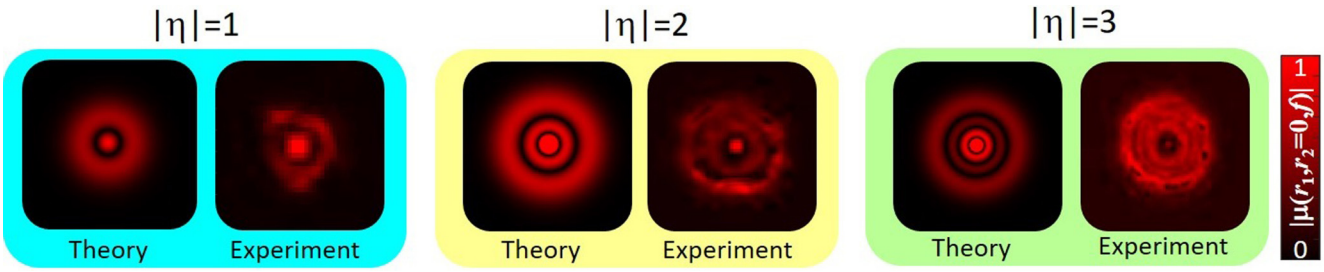

FIG. 10. Distribution of the degree of coherence of different index partially coherent PSVBs ($|\eta| = 1$, 2, and 3) having $\delta = 2.5$ mm under far-field propagation.

intensity modulation and the coherence-induced depolarization in partially coherent PSVBs are found to be dependent on both the input spatial coherence length and PHI ($|\eta|$) of the beam. Also, the DOP profile of a partially coherent PSVB beam on propagation is found to be much different from the isotropic phase vortex beams and vortex-induced radially polarized beams. It is observed that the Gaussian profile of DOC distribution at the source plane evolves into a non-Gaussian profile at the focus. The far-field DOC carries ring-dislocations that are equal to the magnitude of the PHI of the input beam. It is found that in this process of coherence-induced depolarization, the Stokes vortices (S_{12})

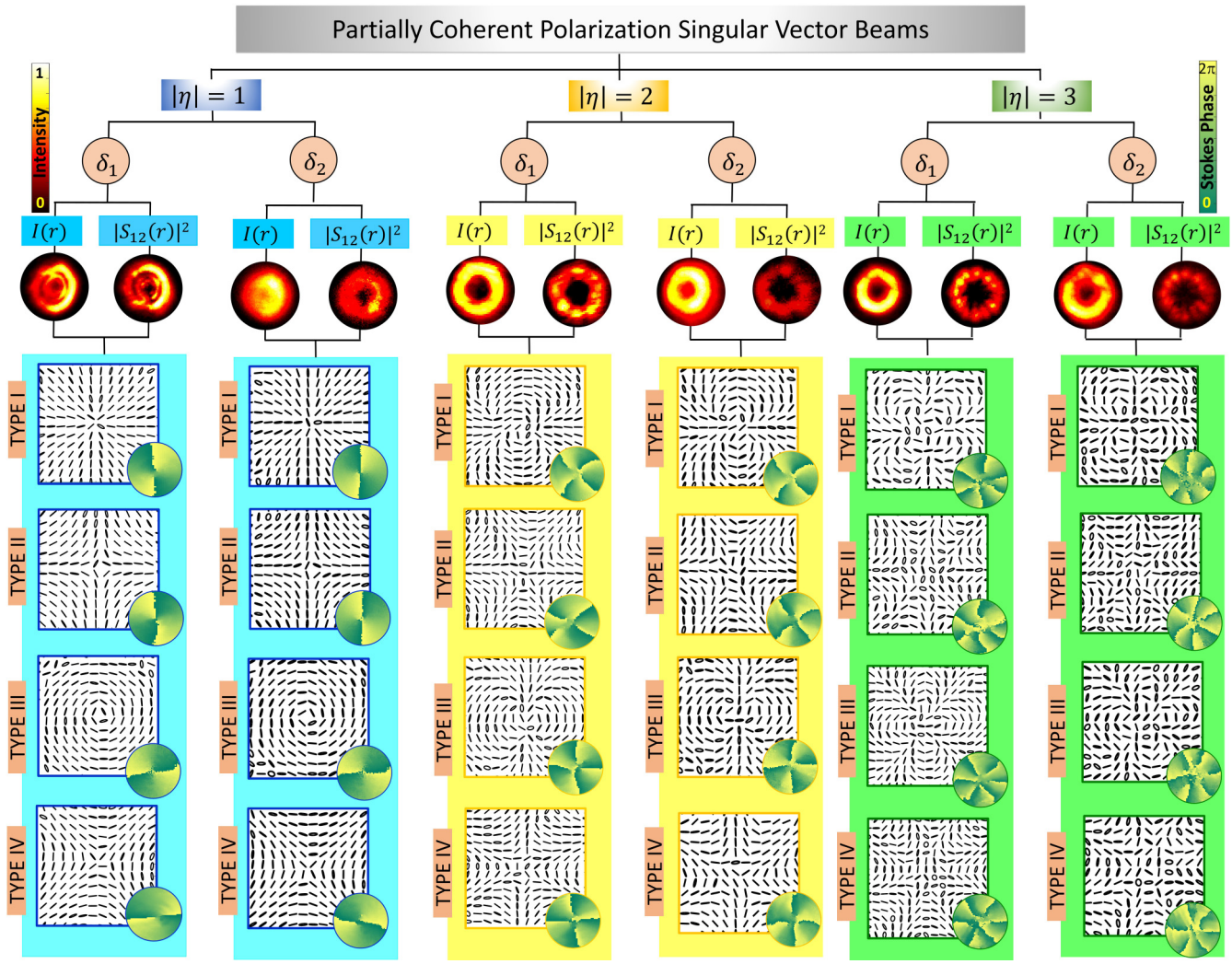

FIG. 11. Experimental results: Degenerate distributions of partially coherent PSVBs of $|\eta| = 1$, 2, and 3, respectively. The SOP distributions of all four types of V-point polarization singularity for a particular $|\eta|$ are also presented corresponding to $\delta_1 = 3.3$ mm and $\delta_2 = 2.3$ mm. The invariance of SOP-distribution on reducing field-correlation (δ) can be observed.

are preserved. The depolarization only results in an enhancement of the unpolarized component that finally modulates the beam-shape and the DOP profile. The associated degeneracy in the intensity profile, the Stokes intensity distribution, and the DOP and DOC profiles for the beams carrying different PHI (or SOP distribution) are also discussed to complete this study. Our results will be useful for trapping and rotating particles, free-space optical communications, and detection of phase objects [18,19,26].

ACKNOWLEDGMENTS

S.J. and S.N.K. acknowledge Indian Institute of Technology Delhi postdoctoral fellowship. This work is supported by Council of Scientific and Industrial Research, India [03(1430)/18/EMR-II and 03(1401)/17/EMR-II] and Department of Science and Technology, India (DST/ICPS/QuST/Theme-I/2019).

[1] E. Wolf, Phys. Lett. A **312**, 263 (2003).
[2] E. Wolf, *Introduction to the Theory of Coherence and Polarization of Light* (Cambridge University Press, Cambridge, 2007).
[3] O. Korotkova and E. Wolf, Opt. Commun. **246**, 35 (2005).
[4] B. Kanseri and H. C. Kandpal, Opt. Lett. **33**, 2410 (2008).
[5] S. Joshi, B. Yadav, M. Verma, M. S. Khan, and H. Kandpal, J. Opt. **15**, 035405 (2013).
[6] M. Verma, P. Senthilkumaran, J. Joseph, and H. Kandpal, Opt. Express **21**, 15432 (2013).
[7] X. Du, D. Zhao, and O. Korotkova, Opt. Express **15**, 16909 (2007).
[8] B. Kanseri, *Optical Coherence and Polarization: An Experimental Outlook* (Lambert Academic, Saarbrücken, 2013).
[9] O. Korotkova, Opt. Commun. **281**, 2342 (2008).
[10] F. Wang, S. Zhu, and Y. Cai, Opt. Lett. **36**, 3281 (2011).
[11] X. Liu, J. Zeng, and Y. Cai, Adv. Phys.: X **4**, 1626766 (2019).
[12] X. Liu, Y. Shen, L. Liu, F. Wang, and Y. Cai, Opt. Lett. **38**, 5323 (2013).
[13] G. Wu, F. Wang, and Y. Cai, Opt. Express **20**, 28301 (2012).
[14] J. Xu and D. Zhao, Opt. Laser Technol. **57**, 189 (2014).
[15] X. Liu, F. Wang, L. Liu, C. Zhao, and Y. Cai, J. Opt. Soc. Am. A **32**, 2058 (2015).
[16] C. Stahl and G. Gbur, J. Opt. Soc. Am. A **34**, 1793 (2017).
[17] Q. Zhan, Opt. Express **12**, 3377 (2004).
[18] G. Arora, Ruchi, and P. Senthilkumaran, Opt. Lett. **45**, 5136 (2020).
[19] C. Rosales-Guzmán, B. Ndagano, and A. Forbes, J Opt. **20**, 123001 (2018).
[20] W. Cheng, J. W. Haus, and Q. Zhan, Opt. Express **17**, 17829 (2009).
[21] K. Khare, P. Lochab, and P. Senthilkumaran, *Orbital Angular Momentum States of Light* (IOP, Bristol, 2020), pp. 2053–2563.
[22] M. Rutkauskas, C. Farrell, C. Dorrer, K. Marshall, T. R. Lundquist, P. Vedagarbha, and D. T. Reid, Opt. Lett. **40**, 5502 (2015).
[23] C. Sun, X. Lv, B. Ma, J. Zhang, D. Deng, and W. Hong, Opt. Express **27**, A245 (2019).
[24] R. Drevinskas, J. Zhang, M. Beresna, M. Gecevičius, A. G. Kazanskii, Y. P. Svirko, and P. G. Kazansky, Appl. Phys. Lett. **108**, 221107 (2016).
[25] A. G. de Oliveira, N. Rubiano da Silva, R. Medeiros de Araújo, P. H. Souto Ribeiro, and S. P. Walborn, Phys. Rev. Appl. **14**, 024048 (2020).
[26] J. Tang, Y. Ming, Z.-X. Chen, W. Hu, F. Xu, and Y. Q. Lu, Phys. Rev. A **94**, 012313 (2016).
[27] P. Senthilkumaran, *Singularities in Physics and Engineering* (IOP, Bristol, 2018), pp. 2053–2563.
[28] E. J. Galvez, Light beams with spatially variable polarization, in *Photonics: Scientific Foundations, Technology and Applications* (Wiley, 2015), Chap. 3, pp. 61–76.
[29] M. Padgett, J. Courtial, and L. Allen, Phys. Today **57**(5), 35 (2004).
[30] Q. Zhan, Adv. Opt. Photon. **1**, 1 (2009).
[31] S. Mamani, L. Shi, D. Nolan, and R. Alfano, J. Biophoton. **12**, e201900036 (2019).
[32] I. Freund, Opt. Commun. **199**, 47 (2001).
[33] I. Freund, Opt. Commun. **201**, 251 (2002).
[34] M. R. Dennis, K. O'Holleran, and M. J. Padgett, in *Progress in Optics* (Elsevier, Amsterdam, 2009).
[35] M. Dong, D. Jiang, N. Luo, and Y. Yang, Appl. Phys. B **125**, 55 (2019).
[36] C. Zhao, Y. Cai, X. Lu, and H. T. Eyyuboğlu, Opt. Express **17**, 1753 (2009).
[37] F. Wang, X. Liu, L. Liu, Y. Yuan, and Y. Cai, Appl. Phys. Lett. **103**, 091102 (2013).
[38] F. Wang, Y. Cai, Y. Dong, and O. Korotkova, Appl. Phys. Lett. **100**, 051108 (2012).
[39] H. Xu, Y. Zhou, H. Wu, H. Chen, Z. Sheng, and J. Qu, Opt. Express **26**, 20076 (2018).
[40] L. Guo, Z. Tang, C. Liang, and Z. Tan, Opt. Laser Technol. **43**, 895 (2011).
[41] Y. Cai, Q. Lin, H. T. Eyyuboğlu, and Y. Baykal, Opt. Express **16**, 7665 (2008).
[42] Y. Dong, F. Wang, C. Zhao, and Y. Cai, Phys. Rev. A **86**, 013840 (2012).
[43] Y. Chen, F. Wang, L. Liu, C. Zhao, Y. Cai, and O. Korotkova, Phys. Rev. A **89**, 013801 (2014).
[44] W. S. Raburn and G. Gbur, Front. Phys. **8**, 168 (2020).
[45] S. Joshi, S. N. Khan, Manisha, P. Senthilkumaran, and B. Kanseri, Opt. Lett. **45**, 4815 (2020).
[46] L. Guo, Y. Chen, X. Liu, L. Liu, and Y. Cai, Opt. Express **24**, 13714 (2016).
[47] J. Zeng, C. Liang, H. Wang, F. Wang, C. Zhao, G. Gbur, and Y. Cai, Opt. Express **28**, 11493 (2020).
[48] B. S. B. Ram, A. Sharma, and P. Senthilkumaran, Opt. Lett. **42**, 3570 (2017).
[49] L. Mandel and E. Wolf, *Optical Coherence and Quantum Optics* (Cambridge University Press, Cambridge, 1995), pp. 428–432.
[50] Q. Lin and Y. Cai, Opt. Lett. **27**, 216 (2002).
[51] A. Jeffrey and H. H. Dai, *Handbook of Mathematical Formulas and Integrals* (Elsevier, Amsterdam, 2008).
[52] G. B. Arfken and H. J. Weber, *Mathematical Methods for Physicists* (Elsevier Academic Press, California, 2005).

[53] F. Cardano, E. Karimi, S. Slussarenko, L. Marrucci, C. de Lisio, and E. Santamato, Appl. Opt. **51**, C1 (2012).
[54] D. F. V. James, J. Opt. Soc. Am. A **11**, 1641 (1994).
[55] J. Tervo, T. Setälä, and A. T. Friberg, Opt. Express **11**, 1137 (2003).
[56] S. N. Khan, S. Deepa, G. Arora, and P. Senthilkumaran, J. Opt. Soc. Am. B **37**, 1577 (2020).
[57] E. Otte, C. Alpmann, and C. Denz, Laser Photon. Rev. **12**, 1700200 (2018).
[58] J. Ou, Y. Jiang, and Y. He, Opt. Laser Technol. **67**, 1 (2015).
[59] J. T. Foley, J. Opt. Soc. Am. A **8**, 1099 (1991).
[60] S. K. Pal, Ruchi, and P. Senthilkumaran, Appl. Opt. **56**, 6181 (2017).
[61] S. Segawa, Y. Kozawa, and S. Sato, Opt. Lett. **39**, 3118 (2014).
[62] Z. Zhao, J. Wang, S. Li, and A. E. Willner, Opt. Lett. **38**, 932 (2013).
[63] B. Ndagano, B. Perez-Garcia, F. S. Roux, M. McLaren, C. Rosales-Guzman, Y. Zhang, O. Mouane, R. I. Hernandez-Aranda, T. Konrad, and A. Forbes, Nat. Phys. **13**, 397 (2017).